

EXPLORING CHANCES AND LIMITATIONS OF HIGH RESOLUTION 3D-PRINTING FOR GUIDED WATER PERCOLATION IN GAS DIFFUSION LAYERS OF POLYMER ELECTROLYTE FUEL CELLS

Tim Dörenkamp¹ , Felix N. Büchi¹ , Thomas J. Schmidt^{1,2} , and Jens Eller¹ 

¹Center for Energy and Environmental Science, Paul Scherrer Institut (PSI), Villigen PSI, Switzerland;

²Institute of Molecular Physical Science, ETH Zürich, Zürich, Switzerland

Correspondence to:

Jens Eller,
jens.eller@psi.ch

How to Cite:

Dörenkamp, T., Büchi, F. N., Schmidt, T. J., & Eller, J. Exploring Chances and Limitations of High Resolution 3D-Printing for Guided Water Percolation in Gas Diffusion Layers of Polymer Electrolyte Fuel Cells. *InterPore Journal*, 1(3), IPJ271124–3.

<https://doi.org/10.69631/ipj.v1i3nr43>

RECEIVED: 12 Sept. 2024

ACCEPTED: 6 Nov. 2024

PUBLISHED: 27 Nov. 2024



@2024 The Authors

ABSTRACT

In polymer electrolyte fuel cells (PEFC), the design of the porous materials is of significant interest due to their crucial role in determining the cell performance. Additive manufacturing (AM) has emerged as a feasible method for producing complex structures, offering precision and customization which cannot be achieved by conventional manufacturing techniques. This study explores the potential of high-resolution 3D-printing to produce gas diffusion layers (GDL) specifically tailored for polymer electrolyte fuel cells. We demonstrate the advantages of the method, such as its ability to create complex features in a 3-dimensional framework, as well as the challenges it faces, including the accuracy, reliability, and handling of the sample. The findings highlight both the promising capabilities and the current limitations of additive manufacturing of GDL, providing insights into future research directions and technological enhancements required to fully leverage AM to produce next generation porous materials.

KEYWORDS

Polymer electrolyte fuel cells PEFC, Water transport, 3D-Printing

This is an open access article published by InterPore under the terms of the Creative Commons Attribution-NonCommercial 4.0 International License (CC BY-NC 4.0) (<https://creativecommons.org/licenses/by-nc/4.0/>).

1. INTRODUCTION

Electrochemical flow cells, such as fuel cells, electrolyzers and redox flow batteries are promising technologies enabling and supporting the strictly necessary decarbonization of the global energy system. They are composed of an anode and a cathode compartment where the oxidation and reduction

reactions take place, respectively. The compartments are separated by a membrane to prevent short circuiting while allowing selective transport of ionic species. The reactants are supplied via flow fields and evenly distributed to the electrode surface by a porous transport layer (PTL), which is implemented between the flow fields and the electrodes. Besides reactant transport, the PTLs need to ensure electrical contact between the electrode and the bipolar plates to facilitate electron transport as well as sufficient thermal conductivity to remove the waste heat along with the exothermal reactions.

In polymer electrolyte fuel cells (PEFC), the design of the PTL, here usually referred to as the gas diffusion layer (GDL), is challenging as it needs to facilitate reactant as well as product water transport while simultaneously removing waste heat and conducting electrons (24). State of the art GDL are made of carbon fibers stacked as papers, felts, or woven materials with fiber diameters of $\sim 10 \mu\text{m}$ and an overall thickness of 100-300 μm , and feature a hydrophobic treatment to improve water management and sustain low saturations during fuel cell operation (30). This is especially critical at high current densities, where inadequate water management can lead to performance decay due to reactant gas starvation (11, 18). Liquid water transport in PEFC is preliminary dominated by capillary forces, as described by the Young-Laplace law, and controlled by either local wettability or pore and throat sizes. Recent studies have explored the potential of using patterned wettability to improve the liquid water evacuation (13, 14, 36, 37), but guiding water percolation on the single pore level by contact angle modifications seems out of reach. Further work has been conducted on modifying the morphology of the GDL, proposing various structures to improve water management in PEFC (1, 9, 10, 29). However, manufacturing and implementing GDLs with precisely defined structures at relevant feature sizes down to less than 10 μm has not yet been achieved.

Over the past decade, efforts in porous media research have been amplified by the development of advanced methods like time resolved 3D-imaging, numerical modeling, and machine learning tools enabling a deeper understanding of transport processes (4). It is essential to further strengthen and extend these efforts to support the development of cost-effective and efficient solutions for sustainable energy conversion to tackle global climate challenges. Recently, additive manufacturing has been explored to design the pore structure of PTLs in various electrochemical flow cell applications. Van der Heijden et. al. (35) utilized carbon lattices received by pyrolysis of a stereolithography (SLA) 3D-printed polymer precursor as porous electrode in vanadium redox-flow batteries. The study demonstrates the potential of 3D printed electrodes to enhance mass transport and reduce pressure drop and recommends future work to further investigate computationally optimized topologies and advanced geometries with increased internal surface areas. Huang et. al. (17) used direct ink writing (DIW) to obtain nickel grid structures implemented as PTLs for anion exchange membrane water electrolysis (AEMWE). They propose that a hierarchical grid gradient structure yields a significant improvement in performance by reducing oxygen bubble adhesion and resident time. Additionally, Beck et. al. (3) used DIW to manufacture carbon-based graphene aerogel flow through electrodes (FTE). Their electrodes exhibit significantly improved mass transfer by leveraging fluid inertia to induce a secondary flow which leads to mass transfer coefficients two orders of magnitude higher compared to previously 3D printed electrodes. Furthermore, Niblett et. al. (27) successfully implemented a 3D-printed pyrolytic carbon GDL produced by constrained surface stereolithography (digital light processing, DLP) and subsequent operation in a polymer electrolyte fuel cell (PEFC), revealing challenges such as membrane and catalyst layer (CL) damage which need to be addressed by improved printing resolution and accuracy.

Among the different printing technologies, DLP is one of the most promising techniques to achieve micrometer sized features and reasonable printing volumes of mm^3/h . Digital light processing utilizes UV-light exposure to cure a photosensitive resin. A mask is projected onto the resin which instantly cures, enabling rapid and accurate layer-by-layer printing. The photosensitive resin is contained in a vat covered by a low adhesive polymer film. The built platform moves up until only a thin layer of resin remains between the polymer film and the platform. The resin is then exposed by the masked UV-light and cures immediately. For the next layer, the platform moves downward, causing the cured resin to detach from the membrane, which allows a new film of resin to spread. The process repeats in consecutive steps until the whole object is formed (6).

Despite its potential, the technology faces several challenges that must be addressed to successfully manufacture GDLs. First, detaching the sample from the polymer film at the end of each printed layer requires overcoming the adhesion force between them, which subjects the sample to mechanical stress. This can cause severe deformations, particularly when printing thin fibrous structures such as GDLs. Extensive work has been conducted to reduce the detachment stress and the impact of different parameters has been investigated. Besides the properties of the membrane and resin, the platform's lifting speed light intensity have been identified as critical parameters (23, 31). Furthermore, during curing, the resin typically undergoes volumetric shrinkage, which can result in dimensional inaccuracies such as curling or warping due to residual internal stress (20, 39). It is reported that some acrylate-based resins can show volume shrinkage of almost 20% during solidification (19). Additionally, the accuracy of the printed part suffers from over-curing effects, which occur when the resin is exposed for too long, causing it to harden excessively. This effect is particularly pronounced in the printing direction, e.g. the direction of light exposure (25). Furthermore, the carbonization of these materials to achieve electrical conductivity is challenging as the degradation of the polymer precursor in a high temperature inert gas atmosphere is associated with an anisotropic volume shrinkage of up to 90%, leading to a dramatic decrease of the volume. It is reported that the orientation during the printing can result in varying degrees of shrinkage in different directions (35).

Recent progress in the field, aimed at enhancing the spatial resolution of DLP printers, have led to the development of projection micro stereolithography (P μ SL), a technology commercialized by Boston Microfabrication Materials Technology Co, Ltd. (BMF) in 2018 (16). Their high resolution MICROARCH® S230 machine can project pixel-sizes down to 2 μ m into a build volume of 50 x 50 x 50 mm with a layer thickness of 5 μ m (5).

In this work, we present a comprehensive analysis of the potential and challenges of high resolution DLP printing for manufacture structured model GDLs with feature sizes as small as 20 μ m. Our goal is to achieve filigree solid structures comparable to today's carbon fiber-based materials and to guide the development of next generation GDLs. Two different structures were printed and tested in an ex-situ liquid injection experiment along with X-ray imaging to track water pathways while simultaneously measuring the pressure in the water phase. Based on these findings, we propose a design for improved liquid water removal through water guidance in PEFCs.

2. METHODOLOGY

2.1. Sample Preparation

The printed structures were designed in Autodesk Inventor 2022 and exported as STL -files to be compatible with the slicing software of the 3D-printer. Slicing, printing and post-processing were done externally by the BMF printing service on a MICROARCH® S230 machine with a pixel resolution of 2 μ m and a layer thickness of 5 μ m. Following printing, the samples were post-cured in a FormCure UV-chamber for 3 h at 60°C. The resin used was BMF HTL-5, which yields a contact angle of 45-60° after printing (5). Hydrophobization of the samples was achieved by drop casting a solution of 0.1 wt% amorphous fluoropolymer^a in Fluorinert™ (FC-70) and drying it in a vacuum oven at a temperature of 80°C for one hour. The solution was prepared by mixing the Teflon particles with the solvent and stirring it at a temperature of 70°C until a clear solution was obtained (38). The contact angle of the coating was probed by using the same coating procedure on a glass substrate and determining the contact angle via sessile droplet method.

2.2. Experimental

The experimental drainage setup which was used is shown in **Figure 1**. The samples were placed in an in-house developed sample holder particularly designed for imbibition and drainage experiments (7, 8).

^a Teflon AF 2400

A clamping tool was used to press the specimen against a fluoroethylene propylene (FEP) film with a stamp and a screw on top of the sample holder, allowing water only to enter through the desired inlet.

A syringe pump^b was used to control the injection rate and a pressure sensor^c was used to measure the pressure of water against a trapped air phase between the liquid surface and the sensor. Image acquisition was performed in a CT scanner^d. Radiographic imaging was done by averaging 2 images recorded at a frequency of 1 Hz and a pixel size of with a spatial resolution of 2.5 μm . Tomographic imaging after liquid injection was done using the fast scan option to achieve scan times of only 1 min with 120 projections of 0.5 s exposure time at a tube voltage of 80 kV, a current of 240 μA and a voxel size of 4 μm . Scanning electron microscopy (SEM) was done with a Zeiss ULTRA 55 at an acceleration voltage of 3 kV. To achieve conductivity for SEM, the sample was sputter-coated with a thin layer of gold.

2.3. Simulation

Capillary pressure curves were simulated using the SatuDict plugin in GeoDict^e. Drainage simulations where a non-wetting phase (here water) invades a pore space filled with a wetting phase (here air) were performed. The constant contact angle approximation was used to define the wetting properties of the structure. Furthermore, the dynamic pore-morphology method with a non-monotonic capillary pressure was employed allowing pressure drop associated with water break-through.

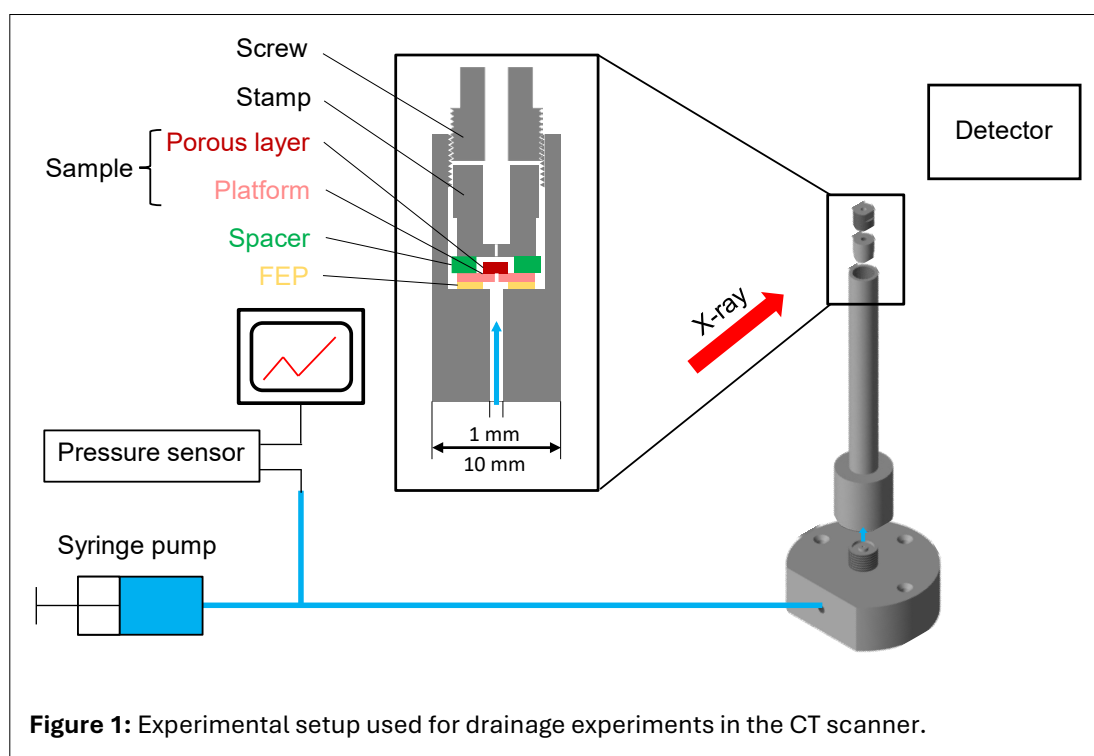


Figure 1: Experimental setup used for drainage experiments in the CT scanner.

^b kdScientific: LEGATO[®] 110

^c Greisinger: GMSD 2 BR, precision ± 1 mbar

^d Phoenix nanotom m: General Electric, Germany

^e Version 2022: Math2Market, Germany

3. RESULTS & DISCUSSION

3.1. P μ SL print quality and limits

To assess the capabilities of the MICROARCH® S230 3D printer, a test object was designed. It featured different structures which are known to be challenging for additive manufacturing, such as thin walls and bridges as well as lattice structures with different feature sizes (see 3D rendering of the tomographic data in **Figure 2a**). The structures were printed together with a supportive base layer to simplify handling, and evaluated by X-ray tomography. First, the machine was tested on its reliability to print solid walls of different thicknesses (5, 10, 20 μm) and up to different heights (max. 200 μm , shown in **Figure 2d**). While the 20 μm thick walls could be printed to the full height without any defects, the thinner walls of 10 μm and 5 μm showed defects when exceeding heights of 50 μm and 20 μm , respectively. It is difficult to say whether the deformation of the thin walls results from detachment stress or general weakness of the structure. In fact, the slightest misalignment of two consecutive printed layers can cause severe deformation and eventually failure of the final structure. Furthermore, bridges over a length of 200 μm (10 times the size of the supporting pillars) could be printed without any problems (see **Figure 2e**). More complex lattice structures exhibiting porous planes stacked on thin pillars were designed, and it was possible to print lattice structures with pillar sizes down to 10 μm and pores of 20 μm (see **Figure 2b**). Limitations were met when trying to scale this structure down to a lattice with 5 μm pillars and pores of 10 μm , which resulted in a solid cube (see the smaller cube in **Figure 2a** which is right next to the enlarged structure in **Figure 2b**).

An intrinsic shortcoming of DLP is the over-curing which is shown in **Figure 2c**. The magnified image on the bottom right shows three successive layers and highlights where the curing was meant to stop.

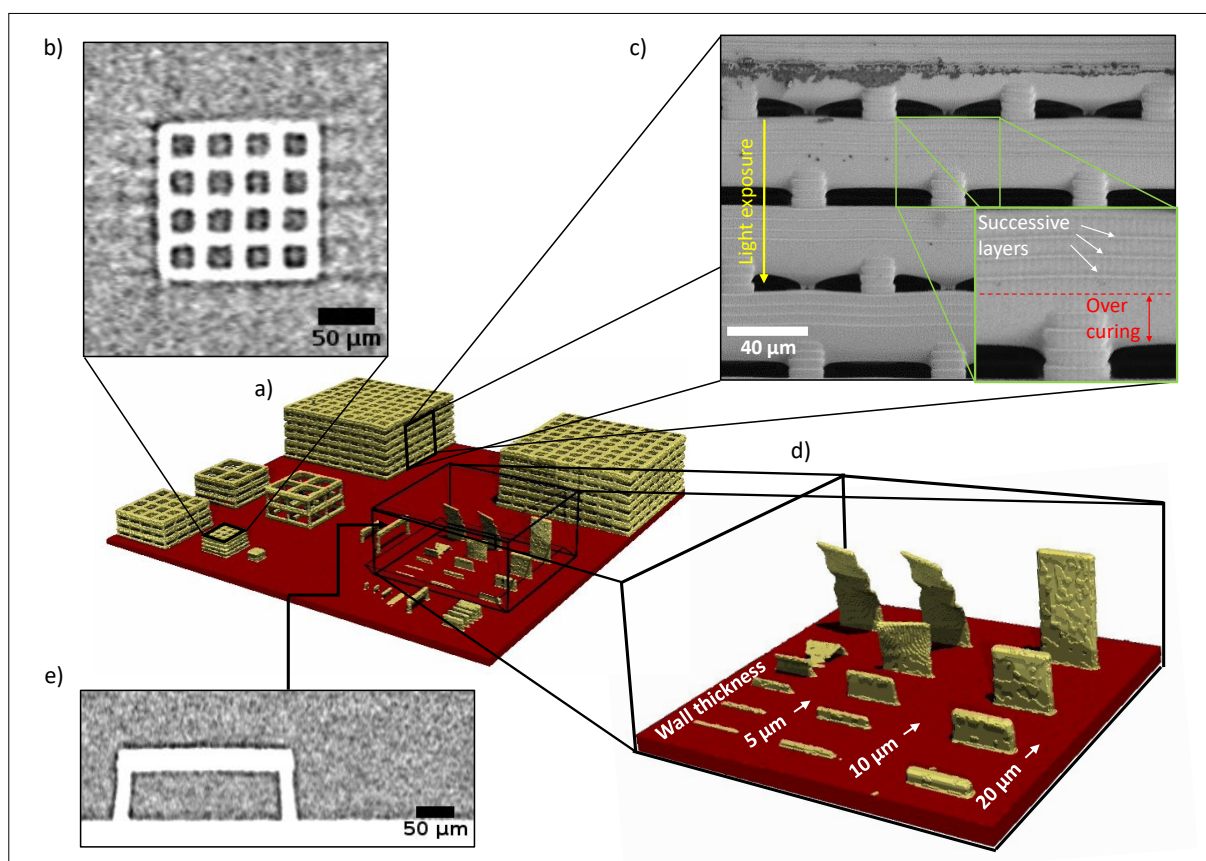


Figure 2: **a)** 3D-rendering of CT scan of the test print showing the different structures (yellow) and the base layer (red). **b)** Tomographic image slice of the smallest resolved lattice structure. **c)** SEM image of the gold coated structure illustrating the over-curing effect (red dashed line depicts where curing should have stopped) with respect to the printing direction and UV-light exposure. **d)** Tomographic image slice showing the longest printed bridge. **e)** 3D-rendering of CT scan of varying wall thicknesses printed up to different heights.

However, the last printed layer exceeded its attempted size ($5\ \mu\text{m}$) by $\sim 15\ \mu\text{m}$. This leads to the conclusion that the highest resolution that can be achieved in the printing direction is $\sim 20\ \mu\text{m}$ when printing one single layer. This has been addressed in later designs, which aimed to print pillars with a quadratic cross-section with an edge length of $20\ \mu\text{m}$ by designing horizontal layers with a thickness of only $5\ \mu\text{m}$ (perpendicular to the printing direction). Similar overcuring factors have also been reported by Niblett et. al. (27) who achieved a minimal feature size of five times the printer resolution with a bottom-up DLP printer.

Table 1: Throat size gradient of the porous structure

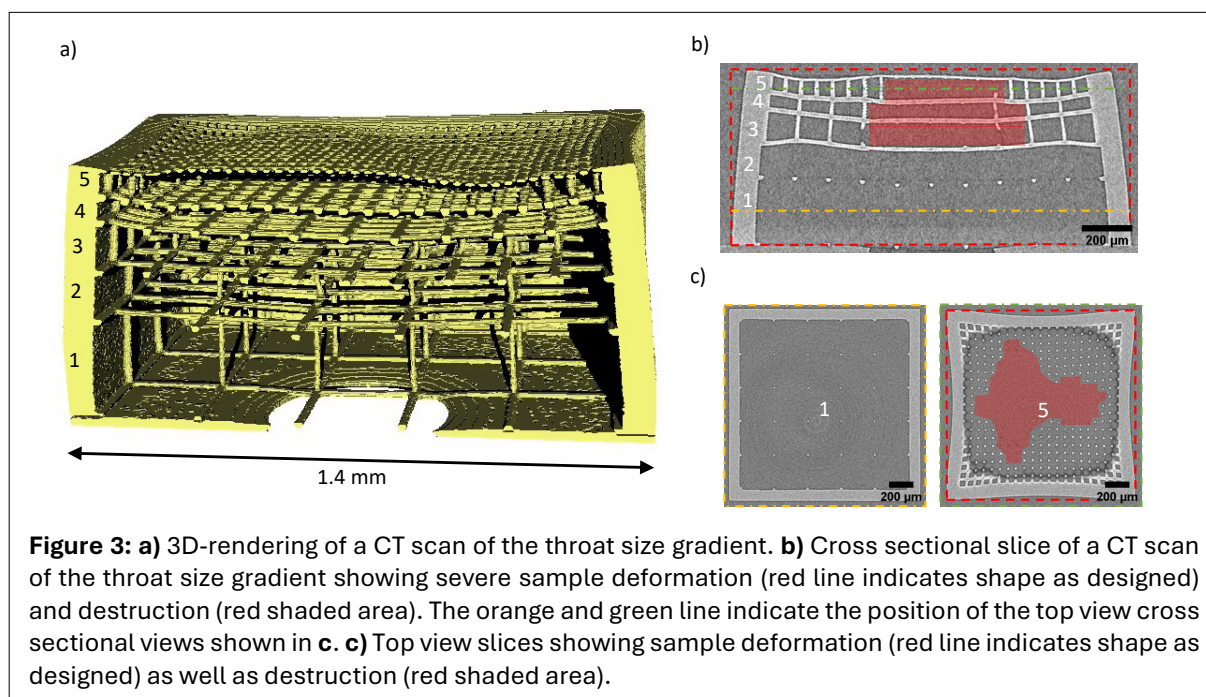
Level	Throat width / μm	Throat length / μm
1	260	260
2	120	260
3	120	120
4	50	120
5	50	50

Our initial attempts to print free-standing GDLs were unsuccessful due to the stress caused during the detachment with a razor blade. Unfortunately, thin pillars in the order of magnitude printed in this work failed to survive this process. Therefore, for subsequent prints, the base layer was retained to facilitate non-destructive sample handling and platform detachment.

After the initial feasibility assessment, P μ SL was used to manufacture lattice structures with narrow and wide throats to explore the potential of using additive manufacturing to create guided water pathways in porous material. A test structure with throat size gradient was printed (see details of throat sizes in Table 1). A 3D rendering of the data obtained from X-ray tomography for one of the printed structures is shown in Figure 3a. It can be observed that the structure suffered severe degrees of deformation, particularly in the last layer (no. 5). The red shaded areas in Figure 3b and Figure 3c illustrate how the regular pattern of vertical pillars were destroyed due to the deformation of the horizontal layers as well as warping of the walls surrounding the lattice, which is indicated by red dashed line which represents the sample shape as it had been designed. According to the observations in this study, the warping becomes worse with sample height. In the fifth layer, almost half of the vertical pillars were not printed. Further samples showed similar defects.

3.2. Break-through pressure vs. throat size

According to the Young-Laplace law, the break-through pressure (p_{BT}) of water draining into a porous medium and displacing the wetting phase (here air) is determined by the size of the throat (r) and the



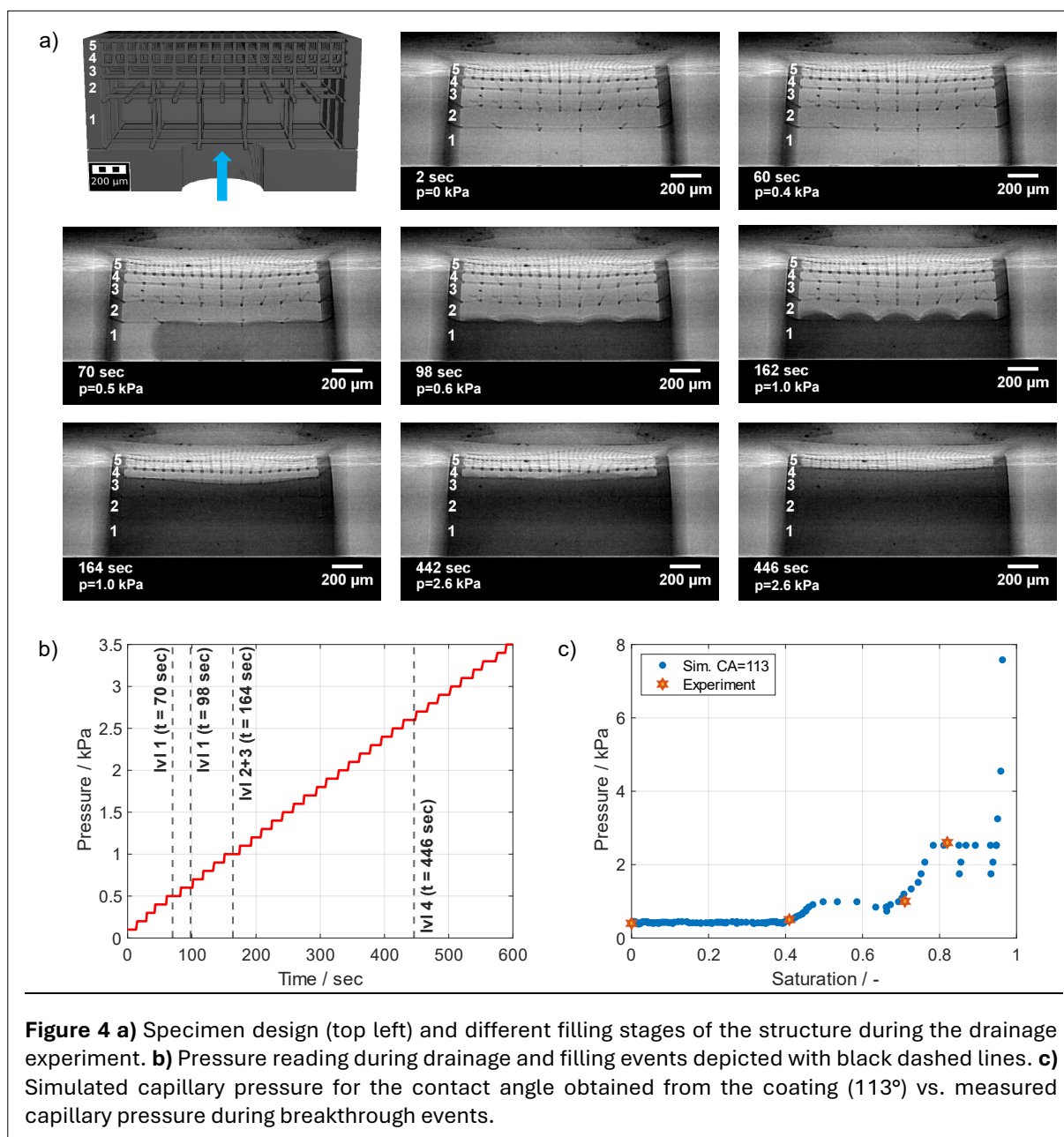
contact angle (θ) of the triple phase boundary between the two fluids and the solid (Eq. 1) where γ represents the surface tension between water and air.

$$p_{BT} = -2\gamma \frac{\cos(\theta)}{r} \quad (1)$$

The contact angle of the surface coating is 113° (measured by sessile droplet on a glass substrate, see Figure S1 in the Supplementary Material, available online), which is close to the reported contact angle of 108° for water on a smooth polytetrafluoroethylene (PTFE) surface (15).

To verify our approach, the break-through pressures were measured during liquid injection into the 3D-printed structure with a throat size gradient. Water was injected upward against the force of gravity as depicted in Figure 4a (top left). The filling height of the water within the structure was captured by X-ray radiography (Figure 4a) while simultaneously measuring the pressure in the system (shown in Figure 4b). The saturation was estimated by the ratio of the filling height over the total sample height.

The pressure in the system increased linearly with time during the injection, with a rate of $5 \mu\text{L}/\text{min}$ defined by the syringe pump. Drainage of the first level ($\sim 0.51 \mu\text{L}$) happened in two consecutive steps, after 70 sec and 98 sec at pressure levels of 0.5 kPa and 0.6 kPa, respectively. This could be explained by



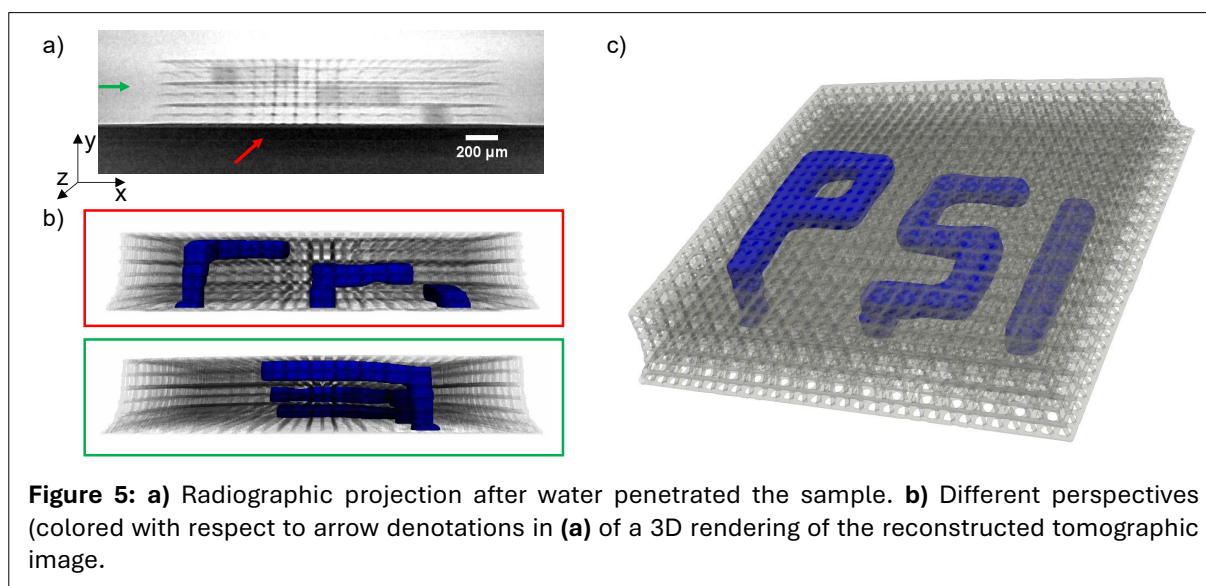
slightly different throat sizes due to inaccuracies of the print, and the time it takes to fill the total volume of the first level. The projection after 162 sec clearly shows a curved water-air interface proving the hydrophobic properties of the structure. After 164 sec, the second and the third level ($\sim 0.39 \mu\text{L}$) filled simultaneously at a pressure of 1 kPa. Note that only the length of the throat is different between those two levels. Level four ($\sim 0.14 \mu\text{L}$) filled after 446 sec at a pressure of 2.6 kPa. Although the throat size between level four and five again only discerns in one dimension, no simultaneous breakthrough was observed in this case. This might be explained by the very poor print quality of the last layer, which exhibited a severe degree of deformation as well as broken fibers, especially in the direction of printing. When referring to **Figure 4c**, it can be observed that the break-through pressure measured in the experiment matches with the one predicted by the capillary invasion simulation with a contact angle of 113° , which is the contact angle that had been observed by sessile droplet. However, this does not hold for level 5, which was predicted to fill at the same pressure as level 4. The liquid injection was stopped after 600 sec to avoid spilling liquid water into the CT scanner.

The break-through pressures in operating fuel cells have been studied for various state of the art materials with average pore sizes in the range of 17-65 μm and large pores up to 200 μm (34). Different experimental ex-situ as well as operando experiments have found break-through pressures in a range of 2-6 kPa that are overlapping with this work for similar pore and throat sizes (2, 22, 26).

3.3. Capillary pressure-controlled water pathways

The relationship between break-through pressure and throat size can be utilized to design preferential routes in a porous medium. As a proof of principle, we designed a structure with a distinguished throat size pattern. The objective was to guide the water from an inlet pool into determined pathways in three directions in the cartesian system (x, y, z) on three different vertical layers individually in the in-plane direction. The structure consists of cubic unit cells with an edge length of 140 μm and throat sizes of 50 μm for water ingress, while throats intended for water break-through have a size of 120 μm (see further design details in **Figure S2**, available [online](#) in the Supplementary Material). For the filling-test, the injection rate of the syringe was set to 2 $\mu\text{L}/\text{min}$. Filling of the structure happened simultaneously at a pressure of 1 kPa, which matches with the break-through pressure obtained from the measurement of the throat size gradient sample. The radiographic projection in **Figure 5a** indicates the water distribution in the sample at the end of the experiment. The 3D information was then captured by X-ray tomography and segmented into three phases (solid, water, air).

The 3D rendering of the segmented data (see **Figure 5b** and **Figure 5c**) reveals the desired percolation pathway of the water into the porous structure and therefore confirms the capability of additive manufacturing to design preferential pathways of two phase flows in PTLs with a high porosity of $\sim 90\%$.

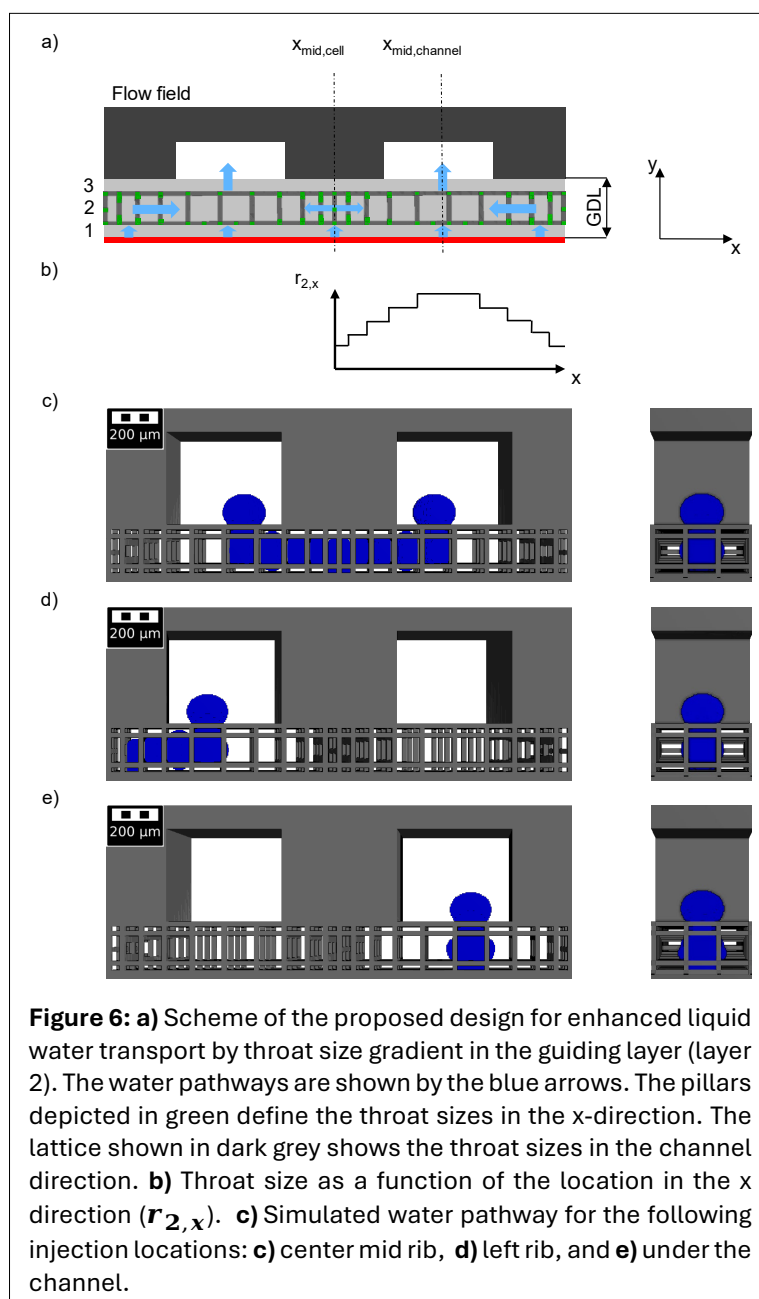


3.4. Percolation pathways designed for PEFC

In PEFC, water is produced in the CL by the oxygen reduction reaction (ORR) and needs to be transported towards the gas channels where it will be dragged to the exhaust by the supply gases. To maximize fuel cell performance, the liquid water saturation in the GDL needs to be minimized, in particular close to the CL. Extending the structured GDLs proposed in literature (28, 29) we propose a three-layered design with a high porosity of $\sim 90\%$ which aims to guide the water from the CL in two dimensions (x and y) into the gas channel and avoid extensive in-plane movement, particularly in the channel direction. A scheme of this design is shown in **Figure 6a**. The objective is to control water percolation through 3 distinct layers (1, 2, 3), to remove water from the CL surface, and force percolation towards the channel where water is dragged away by the reactant gases. For this structure, the percolation of liquid water has only been simulated.

In layer 1, the water moves straight towards the channel to keep the saturation close to the CL as low as possible. This is achieved by throats much larger in the y -direction (xz -plane) compared to the x -direction (xy or yz planes). In the second layer, water percolation is allowed only in the x direction (in-plane). The throat sizes in the x -direction are schematically indicated in **Figure 6b**. The water is expected to always take the shortest straight path towards the region lying perpendicular to the channel. Upon arrival, the water is released into the channel after passing a third layer, which is similar to the first layer and permits only through-plane water percolation in the y -direction. The intention of the third layer is to keep the rib region free from liquid water such that the in-plane pores are always accessible for reactant gas transport.

The proposed schematic design is exemplarily designed for a 0.5/0.5 mm channel/rib configuration and its functionality is shown in a drainage simulation with three different invasion locations (see **Figure 6c, d** and **e**). In the first example, water emerges from the CL in the center of the rib (**Figure 6c**). Due to the symmetric design, the water front in the second layer encounters equal resistance in both x^+ and x^- , which is why the simulation predicts that the water will move towards both directions to the same extent. In a real fuel cell, the first break-through in the second layer will determine whether the water moves in x^+ or x^- since after the first break-through, the pressure required to push through the next adjacent pore becomes lower. This is also shown in the second example where the injection location is under



the left rib, thus the water percolates towards the right (x^+) (Figure 6d). In the last example, the water is coming from a location under the channel and moves directly from the CL into the channel (Figure 6e). The cross section on the right of each case shows that, in none of the tested invasion patterns, does the water percolate along the channel direction. This confirms the effectiveness of the design in achieving the intended 2D water drainage pattern. In the first layer, the water moves into the y -direction away from the CL and into the second layer regardless of where it originated from in the CL. In the second layer, the water moves in the x -direction until it reaches the center of the channel where it then pushes through layer three into the channel. The third layer ensures that water will not accumulate under the rib and therefore secures crossflow between two adjacent channels.

3.5. Outlook towards cell integration and in situ experiments

An overview of the results obtained from the feasibility study is shown in Table 2. To test these structures in operating fuel cells, several issues need to be solved. The filigree solid and highly porous structures required to replace conventional GDL designs, with fiber diameters of about 10 μm , push the limits of, or even exceed the current capabilities of P μ SL technology. However, the authors believe that with extensive studies of process parameters (i.e. lifting speed and exposure time and light intensity), pre-processing steps, and sample handling using an in-house P μ SL printer, many of the print issues can be overcome.

To obtain free standing GDLs, the detachment stress introduced when separating the sample from the built platform after printing needs to be dramatically reduced. This can be achieved by coating the build platform with a sacrificial layer that withstands UV-light exposure and contact with the resin, and can later be dissolved in a solvent. This approach has already been implemented in other studies which struggle with similar processing issues with very small parts produced through two-photon polymerization (TPP). This method enables the realization of printed features on a similar scale with even finer details, which further amplifies the handling issue, but also makes it an alternative candidate to manufacture customized porous GDL structures with enhanced precision (32). Another approach could involve applying a shear force at the interface between the sample and the platform, introduced by the different thermal expansion coefficients of the metal platform and the polymer, by, for instance, freezing of the whole assembly. Future work should also focus on printing structures beyond simple cubic lattices, such as body-centered or face-crossed cubes, which could enhance the stability during printing as well as the mechanical properties of the final structures (12).

Furthermore, electrical conductivity needs to be achieved by either conductive coating or carbonization of the structure. Although pyrolysis is associated with a severe degree of volume shrinkage, and consequently sample de-formation (27, 35), it still seems the more feasible method as sophisticated coating methods like physical vapor deposition (PVD), chemical vapor deposition (CVP) or sputtering are superficial and fail to sufficiently reach every surface in a 3D framework (21). It has been shown in the literature that the resin used for the prints in this work can maintain its structural properties in a pyrolysis process despite volume shrinkage rates of up to 60 % (33). It is of further interest to explore the behavior of different resins in the pyrolysis process to find a candidate with a high carbon yield as well as good structural sustainability and high electrical conductivity after carbonization. To enable in situ experiments on a relevant scale, the sample size and eventually the printing speed need to be increased. The build volume of the printer is 50 x 50 x 50 mm and therefore only capable of printing structures on the differential cell level. With the settings used in this study, it would take more than 9 h to only print one sample with an area of $\sim 1 \text{ cm}^2$ and a thickness of 200 μm . This underlines the strong limitations of additive manufacturing towards real world PEFC application. Currently, the utilization of 3D-printed PTLs in any electrochemical cell remains a research scenario and full

Table 2: Overview of the feasibility assessment of P μ SL to produce GDL for PEFC.

Assessed attribute of P μ SL	✓	(✓)	✗
Resolution	●		
Sample handling			●
Printing speed		●	
Printing volume		●	
Material properties			●

commercialization of those on a stack level seems unreasonable. Nevertheless, with future technology improvements, P μ SL will provide a promising perspective for porous material research.

4. CONCLUSION

This case study on liquid guidance via P μ SL printed model GDL structures reveals the potential as well as the challenges of additive manufacturing for the design of novel porous materials for electrochemical flow cells. We successfully printed highly porous structures with solid matrix features of 20 μ m and pore sizes down to \sim 50 μ m on a support base-layer, which contain defined features to force water percolation into determined pathways based on capillary forces. Based on the results a 2D water percolation design was proposed, which intends to effectively guide liquid water from the CL to the channel in PEFC, as confirmed by simulation.

Despite the potential, several challenges with respect to the printing process, even of small samples (few square mm), were observed. All printed samples had to deal with deformation issues, broken parts, or structural inaccuracies. The minimal achievable feature size was found to be 20 μ m or four times the minimum layer thickness. It was not possible to print and release porous lattice structure directly on the built platform and a supportive base-layer had to instead be introduced. Based on the findings, industrial application of 3D printed GDL is currently not conceivable, but may become viable in the distant future.

Related work should focus on improving the reliability and accuracy of P μ SL to produce model porous materials to study the engineering of water pathways in GDL samples with small feature sizes by characterizing the influence of process parameters, the resin formula and printing speed. Furthermore, for successful cell integration, different routes along with coating and carbonization to achieve electrical conductivity, must be evaluated.

STATEMENTS AND DECLARATIONS

Supplementary Material

Supplementary material on the measurement of the contact angle, and design of the capillary pathways for the "PSI" sample are available [online](#).

Acknowledgements

The authors would like to acknowledge the customer service of Boston Microfabrications (BMF) for technical support, sample manufacturing and post-processing. Thomas Gloor (Paul Scherrer Institut) is acknowledged for his support at the testbench.

Author Contributions

Jens Eller and Tim Dörenkamp: Conceptualization; **Paul Scherrer Institute:** Resources; **Tim Dörenkamp:** Formal analysis; **Jens Eller, Felix N. Büchi, Thomas J. Schmidt:** Supervision; **Tim Dörenkamp:** Investigation, Visualization, Writing – original draft; **all authors:** Methodology, Review & Editing, & final approval of manuscript.

Conflicts of Interest

The authors declare no conflict of interest.

ORCID IDs

Tim Dörenkamp	 https://orcid.org/0000-0002-7233-235X
Felix N. Büchi	 https://orcid.org/0000-0002-3541-4591
Thomas J. Schmidt	 https://orcid.org/0000-0002-1636-367X
Jens Eller	 https://orcid.org/0000-0002-9348-984X

REFERENCES

1. Balakrishnan, M., Shrestha, P., Ge, N., Lee, C., Fahy, K. F., Zeis, R., Schulz, V. P., Hatton, B. D., & Bazylak, A. (2020). Designing tailored gas diffusion layers with pore size gradients via electrospinning for polymer

- electrolyte membrane fuel cells. *ACS Applied Energy Materials*, 3(3), 2695–2707. <https://doi.org/10.1021/acsaem.9b02371>
2. Bazylak, A., Sinton, D., Liu, Z.-S., & Djilali, N. (2007). Effect of compression on liquid water transport and microstructure of PEMFC gas diffusion layers. *Journal of Power Sources*, 163(2), 784–792. <https://doi.org/10.1016/j.jpowsour.2006.09.045>
 3. Beck, V. A., Ivanovskaya, A. N., Chandrasekaran, S., Forien, J.-B., Baker, S. E., Duoss, E. B., & Worsley, M. A. (2021). Inertially enhanced mass transport using 3D-printed porous flow-through electrodes with periodic lattice structures. *Proceedings of the National Academy of Sciences*, 118(32), e2025562118. <https://doi.org/10.1073/pnas.2025562118>
 4. Blunt, M. J., Bazylak, A., Brook, M., Muggeridge, A., & Orr, F. M. (2024). Research needs in porous media for the energy transition. *InterPore Journal*, 1(1), ipj260424-2. <https://doi.org/10.69631/ipj.v1i1nr14>
 5. Boston Microfabrication (BMF) (Document created 30 Jan 2024). HTL Resin Data sheet. <https://bmf3d.com/wp-content/uploads/2024/02/24-BMF-0029-Data-Sheet-Updates-HTL-Resin-PRINT-V2.pdf>
 6. Chaudhary, R., Fabbri, P., Leoni, E., Mazzanti, F., Akbari, R., & Antonini, C. (2023). Additive manufacturing by digital light processing: A review. *Progress in Additive Manufacturing*, 8(2), 331–351. <https://doi.org/10.1007/s40964-022-00336-0>
 7. Chen, Y.-C., Berger, A., De Angelis, S., Schuler, T., Bozzetti, M., Eller, J., Tileli, V., Schmidt, T. J., & Büchi, F. N. (2021). A method for spatial quantification of water in microporous layers of polymer electrolyte fuel cells by x-ray tomographic microscopy. *ACS Applied Materials & Interfaces*, 13(14), 16227–16237. <https://doi.org/10.1021/acsaami.0c22358>
 8. Chen, Y.-C., Karageorgiou, C., Eller, J., Schmidt, T. J., & Büchi, F. N. (2022). Determination of the porosity and its heterogeneity of fuel cell microporous layers by x-ray tomographic microscopy. *SSRN Electronic Journal*. <https://doi.org/10.2139/ssrn.4058912>
 9. Csoklich, C., Steim, R., Marone, F., Schmidt, T. J., & Büchi, F. N. (2021). Gas diffusion layers with deterministic structure for high performance polymer electrolyte fuel cells. *ACS Applied Materials & Interfaces*, 13(8), 9908–9918. <https://doi.org/10.1021/acsaami.0c20896>
 10. Csoklich, C., Xu, H., Marone, F., Schmidt, T. J., & Büchi, F. N. (2021). Laser structured gas diffusion layers for improved water transport and fuel cell performance. *ACS Applied Energy Materials*, 4(11), 12808–12818. <https://doi.org/10.1021/acsaem.1c02454>
 11. Deevanhay, P., Sasabe, T., Tsushima, S., & Hirai, S. (2011). Investigation of water accumulation and discharge behaviors with variation of current density in PEMFC by high-resolution soft X-ray radiography. *International Journal of Hydrogen Energy*, 36(17), 10901–10907. <https://doi.org/10.1016/j.ijhydene.2011.05.160>
 12. Egan, P., Wang, X., Greutert, H., Shea, K., Wuertz-Kozak, K., & Ferguson, S. (2019). Mechanical and biological characterization of 3D printed lattices. *3D Printing and Additive Manufacturing*, 6(2), 73–81. <https://doi.org/10.1089/3dp.2018.0125>
 13. Forner-Cuenca, A., Biesdorf, J., Lamibrac, A., Manzi-Orezzoli, V., Büchi, F. N., Gubler, L., Schmidt, T. J., & Boillat, P. (2016). Advanced water management in PEFCs: Diffusion layers with patterned wettability: II. Measurement of capillary pressure characteristic with neutron and synchrotron imaging. *Journal of The Electrochemical Society*, 163(9), F1038–F1048. <https://doi.org/10.1149/2.0511609jes>
 14. Forner-Cuenca, A., Manzi-Orezzoli, V., Biesdorf, J., Kazzi, M. E., Streich, D., Gubler, L., Schmidt, T. J., & Boillat, P. (2016). Advanced water management in PEFCs: Diffusion layers with patterned wettability: I. Synthetic routes, wettability tuning and thermal stability. *Journal of The Electrochemical Society*, 163(8), F788–F801. <https://doi.org/10.1149/2.0271608jes>
 15. Fox, H. W., & Zisman, W. A. (1950). The spreading of liquids on low energy surfaces. I. polytetrafluoroethylene. *Journal of Colloid Science*, 5(6), 514–531. [https://doi.org/10.1016/0095-8522\(50\)90044-4](https://doi.org/10.1016/0095-8522(50)90044-4)
 16. Ge, Q., Li, Z., Wang, Z., Kowsari, K., Zhang, W., He, X., Zhou, J., & Fang, N. X. (2020). Projection micro stereolithography based 3D printing and its applications. *International Journal of Extreme Manufacturing*, 2(2), 022004. <https://doi.org/10.1088/2631-7990/ab8d9a>
 17. Huang, B., Wang, X., Li, W., Tian, W., Luo, L., et al. (2023). Accelerating gas escape in anion exchange membrane water electrolysis by gas diffusion layers with hierarchical grid gradients. *Angewandte Chemie*, 135(33), e202304230. <https://doi.org/10.1002/ange.202304230>
 18. Ihonen, J., Mikkola, M., & Lindbergh, G. (2004). Flooding of gas diffusion backing in PEFCs. *Journal of The Electrochemical Society*, 151(8), A1152. <https://doi.org/10.1149/1.1763138>
 19. Jian, Y., He, Y., Jiang, T., Li, C., Yang, W., & Nie, J. (2012). Polymerization shrinkage of (Meth)acrylate determined by reflective laser beam scanning. *Journal of Polymer Science Part B: Polymer Physics*, 50(13), 923–928. <https://doi.org/10.1002/polb.23086>

20. Karalekas, D., & Aggelopoulos, A. (2003). Study of shrinkage strains in a stereolithography cured acrylic photopolymer resin. *Journal of Materials Processing Technology*, 136(1–3), 146–150. [https://doi.org/10.1016/S0924-0136\(03\)00028-1](https://doi.org/10.1016/S0924-0136(03)00028-1)
21. Lakhtakia, A., & Martín-Palma, R. J. (Eds.). (2013). Engineered biomimicry. In: *Engineered Biomimicry* (p. i). Elsevier. <https://doi.org/10.1016/B978-0-12-415995-2.00019-2>
22. Lamibrac, A., Roth, J., Toulec, M., Marone, F., Stampanoni, M., & Büchi, F. N. (2016). Characterization of liquid water saturation in gas diffusion layers by x-ray tomographic microscopy. *Journal of The Electrochemical Society*, 163(3), F202–F209. <https://doi.org/10.1149/2.0401603jes>
23. Li, X., Kang, X., Xiao, H., & Duan, Y. (2022). Low adhesion continuous constrained-surface projection stereolithography process based on curing degree control. *Additive Manufacturing*, 54, 102743. <https://doi.org/10.1016/j.addma.2022.102743>
24. Mathias, M.F., Roth, J., Fleming, J. and Lehnert, W. (2010). Diffusion media materials and characterisation. In: *Handbook of Fuel Cells*. John Wiley & Sons, Ltd. Print ISBN: 9780470741511| Online ISBN: 9780470974001| <https://doi.org/10.1002/9780470974001.f303046>
25. Melchels, F. P. W., Feijen, J., & Grijpma, D. W. (2010). A review on stereolithography and its applications in biomedical engineering. *Biomaterials*, 31(24), 6121–6130. <https://doi.org/10.1016/j.biomaterials.2010.04.050>
26. Mularczyk, A., Lin, Q., Niblett, D., Vasile, A., Blunt, M. J., Niasar, V., Marone, F., Schmidt, T. J., Büchi, F. N., & Eller, J. (2021). Operando liquid pressure determination in polymer electrolyte fuel cells. *ACS Applied Materials & Interfaces*, 13(29), 34003–34011. <https://doi.org/10.1021/acsami.1c04560>
27. Niblett, D., Guo, Z., Holmes, S., Niasar, V., & Prosser, R. (2022). Utilization of 3D printed carbon gas diffusion layers in polymer electrolyte membrane fuel cells. *International Journal of Hydrogen Energy*, 47(55), 23393–23410. <https://doi.org/10.1016/j.ijhydene.2022.05.134>
28. Niblett, D., Mularczyk, A., Niasar, V., Eller, J., & Holmes, S. (2020). Two-phase flow dynamics in a gas diffusion layer—Gas channel—Microporous layer system. *Journal of Power Sources*, 471, 228427. <https://doi.org/10.1016/j.jpowsour.2020.228427>
29. Niblett, D., Niasar, V., & Holmes, S. (2020). Enhancing the performance of fuel cell gas diffusion layers using ordered microstructural design. *Journal of The Electrochemical Society*, 167(1), 013520. <https://doi.org/10.1149/2.0202001JES>
30. Okonkwo, P. C., & Otor, C. (2021). A review of gas diffusion layer properties and water management in proton exchange membrane fuel cell system. *International Journal of Energy Research*, 45(3), 3780–3800. <https://doi.org/10.1002/er.6227>
31. Pan, Y., He, H., Xu, J., & Feinerman, A. (2017). Study of separation force in constrained surface projection stereolithography. *Rapid Prototyping Journal*, 23(2), 353–361. <https://doi.org/10.1108/RPJ-12-2015-0188>
32. Soreni-Harari, M., St. Pierre, R., McCue, C., Moreno, K., & Bergbreiter, S. (2020). Multimaterial 3D printing for microrobotic mechanisms. *Soft Robotics*, 7(1), 59–67. <https://doi.org/10.1089/soro.2018.0147>
33. Taale, M., Schamberger, B., Monclus, M. A., Dolle, C., Taheri, F., Mager, D., Eggeler, Y. M., Korvink, J. G., Molina-Aldareguia, J. M., Selhuber-Unkel, C., Lantada, A. D., & Islam, M. (2024). Microarchitected compliant scaffolds of pyrolytic carbon for 3D muscle cell growth. *Advanced Healthcare Materials*, 13(9), 2303485. <https://doi.org/10.1002/adhm.202303485>
34. Xu, H., Bühner, M., Marone, F., Schmidt, T. J., Büchi, F. N., Eller, J. (2021). Effects of Gas Diffusion Layer Substrates on PEFC Water Management: Part I. Operando Liquid Water Saturation and Gas Diffusion Properties. *Journal of The Electrochemical Society*, 168, 074505. <https://doi.org/10.1149/1945-7111/ac1035>
35. Van Der Heijden, M., Kroese, M., Borneman, Z., & Forner-Cuenca, A. (2023). Investigating mass transfer relationships in stereolithography 3d printed electrodes for redox flow batteries. *Advanced Materials Technologies*, 8(18), 2300611. <https://doi.org/10.1002/admt.202300611>
36. Wang, X. L., Qu, Z. G., Lai, T., Ren, G. F., & Wang, W. K. (2022). Enhancing water transport performance of gas diffusion layers through coupling manipulation of pore structure and hydrophobicity. *Journal of Power Sources*, 525, 231121. <https://doi.org/10.1016/j.jpowsour.2022.231121>
37. Wen, Q., Pan, S., Li, Y., Bai, C., Shen, M., Jin, H., Ning, F., Fu, X., & Zhou, X. (2022). Janus gas diffusion layer for enhanced water management in proton exchange membrane fuel cells (PEMFCs). *ACS Energy Letters*, 7(11), 3900–3909. <https://doi.org/10.1021/acsenergylett.2c02012>
38. Zalitis, C. M., Kramer, D., & Kucernak, A. R. (2013). Electrocatalytic performance of fuel cell reactions at low catalyst loading and high mass transport. *Physical Chemistry Chemical Physics*, 15(12), 4329. <https://doi.org/10.1039/c3cp44431g>
39. Zhang, Q., Weng, S., Hamel, C. M., Montgomery, S. M., Wu, J., Kuang, X., Zhou, K., & Qi, H. J. (2021). Design for the reduction of volume shrinkage-induced distortion in digital light processing 3D printing. *Extreme Mechanics Letters*, 48, 101403. <https://doi.org/10.1016/j.eml.2021.101403>